ANALYSIS OF GROUND MOTIONS RECORDED DURING THE 2019 RIDGECREST EARTHQUAKE SEQUENCE

Silvia Mazzoni[1], Sean K. Ahdi[1], Tadahiro Kishida[2], Pengfei Wang[1], Chukwuebuka C. Nweke[1], Nicolas Kuehn[1], Victor Contreras[1], Jonathan P. Stewart[1], and Yousef Bozorgnia[1]

1. University of California, Los Angeles, Los Angeles, California
2. Department of Civil Infrastructure and Environmental Engineering, Khalifa University of Science and Technology, Abu Dhabi, United Arab Emirates

Abstract

We summarize an analysis of ground motions recorded during three events that occurred during the July 2019 Ridgecrest earthquake sequence. We collected and uniformly processed 1,483 three-component recordings for the events from an array of 824 sensors spanning ten seismographic networks. Signal processing followed well-established NGA procedures. We developed site condition metadata from available geophysical data and multiple models. We computed intensity measures such as spectral acceleration at a number of oscillator periods and inelastic response spectra. We compared elastic and inelastic response spectra to seismic design spectra in building codes to evaluate ground motion damage potential at spatially-distributed sites.

Introduction

The three events of the 2019 Ridgecrest earthquake sequence started at 10:33 AM local time on July 4, 2019, with a moment magnitude (**M**) 6.5 event located south of China Lake and west of Searles Valley, California. This **M**6.5 event occurred on a left-lateral NE-trending fault (roughly parallel with the Garlock fault to the south) at a hypocentral depth of 10.5 km. This earthquake was followed on July 5 by a **M**5.5 event at 4:07 AM local time at a hypocentral depth of 7.0 km, and a **M**7.1 event at 8:19 PM local time, the latter on a NW-trending right-lateral fault at a depth of 8.0 km (GEER [2019]). These events occurred on faults within the formerly-named greater Little Lake fault zone, but have now been differentiated after the recent earthquakes and are referred to as the Salt Wells Valley fault zone (for the **M**6.5 event; DuRoss et al. [2020]), and the Paxton Ranch fault zone (for the **M**7.1 event; DuRoss et al. [2020]). Since they were proximal in space and time, the **M**6.5 and **M**5.5 events are considered to be foreshocks to the **M**7.1 event (Ahdi, et al., 2020).

In this paper, we present a summary of recorded and processed ground motions, independent (measured) metadata, including information describing the recording stations (sites), and dependent (computed) data and metadata, such as various source-to-site distance metrics and directivity parameters, and computed elastic and inelastic response spectra. The response spectra are compared to the design spectra at each recording station to understand geographic trends. All data are publicly available from the UCLA Natural Hazards Risk and Resiliency Research Center (NHR3), as described in a report by Ahdi et al. (2019). A more complete version of this

paper has been previously published by Ahdi et al. (2020).

Compilation of Site Metadata

Seismological parameters such as magnitude, style of faulting, and fault geometry were reviewed and compiled to facilitate ground motion studies, including calculation of multiple distance metrics such as the epicentral, hypocentral, rupture, and Joyner-Boore distance (closest distance from site to the surface projection of the fault surface). The selection and computation of these parameters is described in Ahdi et al. (2020). The following subsections elaborate on the estimation of site parameters for recording sites.

A site database (SDB) was developed, encompassing information such as (where available for each station) network code, station location information (latitude, longitude, and elevation), information on the time-averaged shear-wave velocity (V_S) in the upper 30 m (V_{S30}) obtained from both measured V_S profiles and from proxy-based V_{S30} estimates, and basin depth parameters (z_x), which are measured as the vertical distance from the ground surface to the first encounter of $x = 1.0$, 1.5, and 2.5 km/s V_S horizons.

Estimation of V_{S30} at Recording Stations

Figure 1 shows a map of stations in the SDB with site markers color-coded by NEHRP site classes. V_{S30} values were assigned based on the availability of measured V_S profiles from geophysical measurements proximate (< 300 m) to the recording station. Profile data was queried from the Community Shear Wave Velocity Profile Database of Ahdi et al. (2018). When measured V_{S30} values are unavailable, V_{S30} is assigned based on various proxy-based models, including those based on surficial geology, topographic slope, and geomorphic terrain classifications.
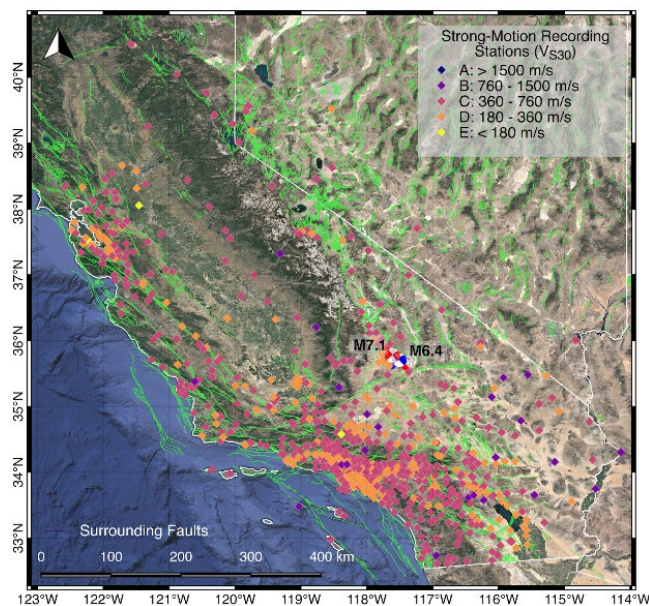

Figure 1. Spatial distribution of recording stations in the ground motion database. Stations are color-shaded according to V_{S30}-based NEHRP site class (Ahdi, et al., 2020).

The following protocol was used in assigning V_{S30} values for a given station:

1. Consider available published databases of measured V_S profiles and V_{S30} values:
   - United States Community V_S Profile Database (PDB, Ahdi et al., 2018), which includes data from the USGS V_{S30} Compilation (Yong et al., 2016)
   - NGA-West2 Site Database (Seyhan et al., 2014)
   - Center for Engineering Strong Motion Data (CESMD, 2019)
2. Match available measured V_{S30} values from all databases to station of interest by computing the distances between the station and the locations of the V_{S30} measurement, and take the closest measurement (using a 300-m cutoff distance) if there are multiple available measurements that do not match the station coordinates exactly (i.e., distance = 0 m).
3. Use proxy-based V_{S30} estimation models if:
   a. There exists no V_{S30} measurement within 300 m of the station; or
   b. The only measured V_{S30} within 300 m of the station was obtained using the Refraction Microtremor (ReMi™) method (Louie, 2001).

Descriptions of various geophysical methods used to obtain V_S profiles are beyond the scope of this paper, but we largely followed the guidelines set forth in V_S data attribution as outlined in Ahdi et al. (2018). The SDB includes 824 recording stations. A total of 203 (25%) stations have measured V_{S30} values, and for the remaining 621 stations, V_{S30} values are inferred using proxy-based methods (described below).

For sites lacking in-situ V_{S30} measurements, one or more of the following four proxy-based models was utilized:

1. krig: a Kriging-based regression map informed by measured V_{S30} data and a hybrid geology-topographic slope model. The Kriging approach is from Thompson et al. (2014) and Thompson (2018), and the hybrid model is from Wills et al. (2015);
2. terr: geomorphic terrain proxy model (Yong, 2016) based on terrain classes from Iwahashi and Pike (2007);
3. slp: topographic slope-based model (Wald and Allen, 2007).

To compute the model output, all sites in the SDB were assigned the relevant values of terrain classes or topographic slope gradients or were plotted on the raster map for the krig model. Figure 2 illustrates the assignment of V_{S30} based on these parameters. The krig model is preferred due to its inclusion of measured V_{S30} values, and thus is utilized wherever data falls within the geographic extent of the model (i.e., the state of California). Weights of 2/3 and 1/3 were applied for sites using both the krig and terr models, respectively. All inferred V_{S30} values from proxy-based models used the krig or krig-terr pair of models, except for 10 sites located in Nevada for which the kriging map is not defined, and one site (CGS station number 13877) which plots in the water due to the relatively coarse resolution of the kriging map and the 1-km spacing of the terrain classifications.

Estimation of Basin Depth Terms at Recording Stations

The z_x parameters were obtained by querying the Unified Community Velocity Models (CVMs) provided by the Southern California Earthquake Center (SCEC; Small et al., 2017). Values were obtained by querying a meta-model, which is a tiled system of multiple velocity models. For this project, the meta-model consisted of five velocity models, which are defined in Table 4 of Ahdi et al. (2020) based on a framework developed in Nweke et al. (2018). The tiled system uses latitude and longitude coordinates to query the CVMs in order of their designated priority. If the coordinates fall within the geographical extents of a model, then the appropriate z_x value will be selected (Small et al., 2017). If the coordinate falls outside the geographical extents of the given model, the next CVM in the tiled order will be checked, and the process is repeated until a CVM is encountered that encompasses the location of interest. To account for locations outside the boundary region of the velocity models in the meta-model, a background 1D velocity model is placed last in the tiled structure as it covers the largest area and serves as a supporting model to the standard CVMs. If a site's coordinates were to fall outside of all tiled CVM extents, the site is not assigned a z_x value. For this dataset, all 824 stations fell within the extent of the tiled CVMs and were thus assigned z_x values. When the model output for a site yields $z_{1.0} = 0$, we check against geological maps. Zero depth is retained for sites located on mapped hard rock geology (crystalline rock, Cretaceous rock, or volcanic rock units), and $z_{1.0}$ is indicated as undefined if the geology is mapped as Tertiary rock or sediments.
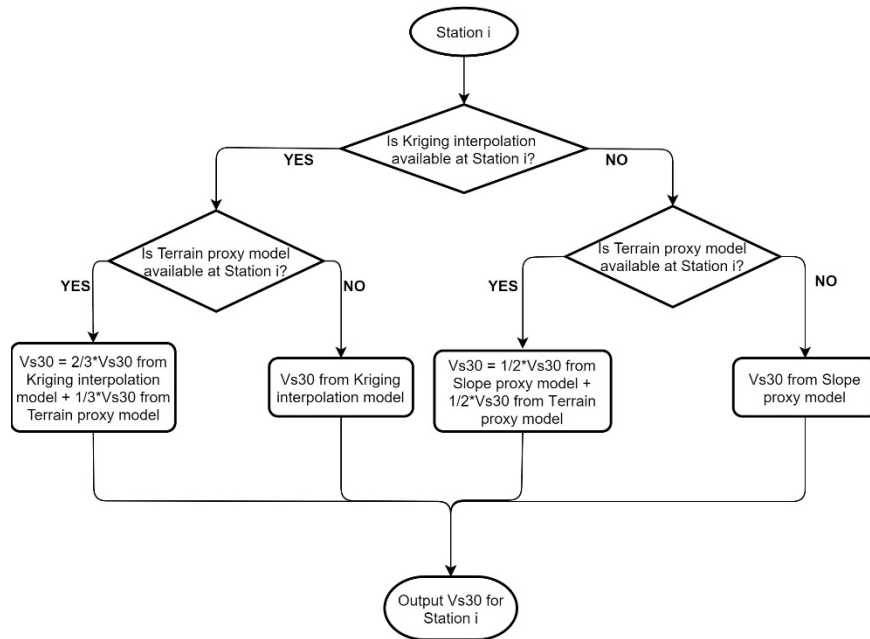

Figure 2. Flowchart depicting logic for assignments for proxy-based V_{S30} values in absence of measurements within proximity to station (see Ahdi, et al., 2020). Note that the geo model (hybrid geology-slope proxy model of Wills et al. 2015) was not considered on its own, as it is a basis for the map used in the kriging-based model of Thompson (2018).

Ground-Motion Intensity Measures

Elastic response spectra were computed for the time series collected for the three main events, including the three individual as-recorded components (H1, H2, and V), the RotD50 and RotD100 components, and the fault-parallel and fault-normal components of the records in the vicinity of the faults. RotD50 and RotD100 are defined by Boore (2010). Figure 3 shows an example of these intensity measures for the site CLC located 2 km from the **M**7.1 rupture, as compared to ground motion models (GMMs) and code-based values. Figure 3a (top left) compares the RotD50 component to predictions from the NGA-West2 GMMs. More comparison cases are provided in Ahdi et al. (2020). Figure 3b compares the RotD100 component to the ASCE 7-10 mapped design values—the Risk-Targeted Maximum Considered Earthquake, MCE_R, and the Design Earthquake, DE (DE = 2/3 * MCE_R), adjusted for its site class (ASCE, 2010, 2016). This comparison shows that the Ridgecrest **M**7.1 mainshock exceeded the Design-Earthquake spectrum at this location for most structural periods. Figure 3c compares the response spectrum of the three as-recorded components to the maximum component (RotD100). The H1 horizontal direction has the highest spectral demand for all periods. Figure 3d compares the response spectra for the FP and FN components to the maximum component shown in Figure 3c. At this location, the FP component carries most of the energy at long periods. These rotated components are valuable to studies of near-fault effects and provide insight on ground motion polarization.

Damage Potential of Recorded Ground Motions

In this section we present a summary of response of a generic single-degree-of-freedom (SDOF) inelastic system to the recorded ground motions. Inelastic analyses of representative structural types using the recorded ground motions provide an opportunity to draw different insights into the geographic distribution of expected generic inelastic-structure response and damage potential in the area affected by the seismic event (Ahdi, et al, 2020). These analyses were performed on a generalized inelastic SDOF model using OpenSees (McKenna et al., 2010). The main feature of an inelastic model is its ability to capture strength reduction and softening due to yielding, as well as hysteretic energy dissipation. The "yield strength" of the SDOF is based on the strength reduction factor (R_d), defined as the ratio between the lateral-force strength for design and the yield strength of the structure, V_y. This value is equivalent to a combination of the strength-reduction factor R and the overstrength factor used in seismic structural design. The typical range for R_d is between 0.5 and 4. When $R_d = 1$, the structure will yield at the DE level. When $R_d > 1$, the structure will yield when subjected to a below-design-level earthquake. When $R_d < 1$, the structure will remain elastic at and below the DE (Ahdi, et al, 2020). The estimated yield strength of the structure is, thus, defined as a function of the design spectrum at the site. The ASCE 7-10 MCE_R spectrum (ASCE, 2010) was obtained for each recording station via the USGS Design-Maps Web-Services tools. Either the ASCE 7-10 standard or ASCE 7-16 specification (ASCE, 2016) could be used; we used the former as it does not require site-specific analyses for softer soil conditions, which would prevent uniform and automated application of the current methodology to all recording stations presented herein. Two values of R_d were chosen for the analyses ($R_d = 2$ and 4). These values are expected to represent structures designed to an R-factor between 4 and 8.
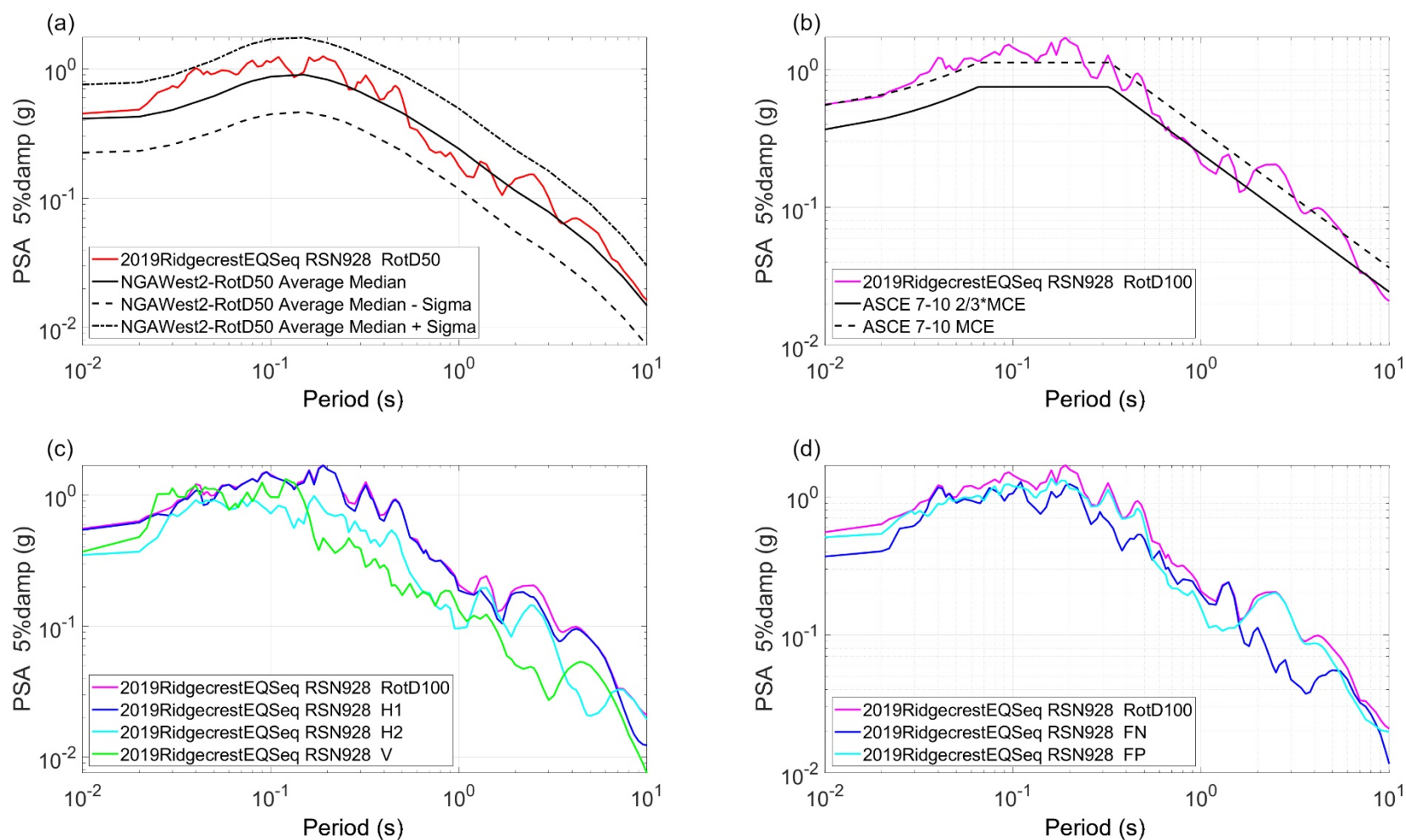
Figure 3. Example plots from the **M**7.1 event for site CLC of (a) observed RotD50 response spectrum compared with the average of the five NGA-West2 predictions; (b) observed RotD100 response spectrum as compared with the ASCE 7-10 MCE$_R$ spectrum and DE (= 2/3 MCE$_R$) spectrum; (c) observed RotD100, H1, H2, and V response spectra; and (d) observed RotD100, fault-normal (FN) and fault-parallel (FP) response spectra (Ahdi, et al., 2020).

Both inelastic and elastic responses of the SDOF system were computed for all the recordings for the **M**7.1 event for both periods and strength levels. For the elastic case, a damping ratio of 5% was used, which is common in engineering practice. For the inelastic case, a reduced damping ratio of 2% was utilized, as the hysteretic energy dissipation is already captured in these nonlinear analyses as compared to the elastic case, which leverages a higher viscous damping ratio in order to partly capture the hysteretic damping which is not explicitly modeled therein.

An example of the inelastic response parameters is mapped for T = 1.0 s in Figure 4 for R_d = 2. The figure consists of 4 maps. The first map, on the top left shows the geographic distribution of the maximum elastic-deformation demand (S_d). The data in this map is the same for both cases of R_d. The second map, on the top right, plots the geographic distribution of D_y, which is defined by expected strength evaluated from the R_d factor and the ASCE 7-10 MCE spectra. The map on the bottom left shows the geographic distribution of the inelastic-deformation demands (D_{max}). The normalized deformation demands show that there are different regions with different levels of expected response, both near and far from the epicenter. The patterns shown in the damage-potential maps show that distance and site conditions are not the only response parameters. Details of such analysis can be found in Ahdi, et al. (2020).

Predicted versus Observed Response Spectra

A comparison of the PSA values computed based on the recorded ground motions and those predicted by the NGA-West2 GMMs was carried out. Figure 3a shows an example of such comparisons for the **M**7.1 event at site CLC. Five NGA-West2 models were considered: Abrahamson et al. (2014), Boore et al. (2014), Campbell and Bozorgnia (2014), Chiou and Youngs (2014), and Idriss (2014); hereafter ASK, BSSA, CB, CY, and ID, respectively.

Ahdi et al. (2020) analyzed residuals (difference between natural log of computed intensity measure and NGA-West2 model medians) to evaluate potential biases in the modeling of source, path, and site effects. Figure 5 shows an example of the average residuals for the **M**7.1 event. Ahdi et al. (2020) present the same plot for the other two events, which are omitted here for brevity. All residuals are slightly positive for the two larger events at short periods. At longer periods, average residuals increase, perhaps due to under-prediction of basin depth scaling by the GMMs.

Summary

A summary of analysis of the ground motions recorded in the 2019 Ridgecrest earthquake sequence is presented. The metadata pertaining to the earthquake source, such as finite-fault solutions, seismic site information including V_{S30} and basin depths, and wave-propagation path distances are compiled. We utilize a relational database to organize and store all data. Comparisons of the response spectra of the recorded ground motions to those of the NGA-West2 GMMs show on average favorable model performance. The large number of recordings and the dense distribution of the recordings in a region that is crossed by significant faults has allowed us to compute intensity measures beyond elastic response spectra so that we can quantify the expected distribution of damage in areas of varying seismic demands (both near
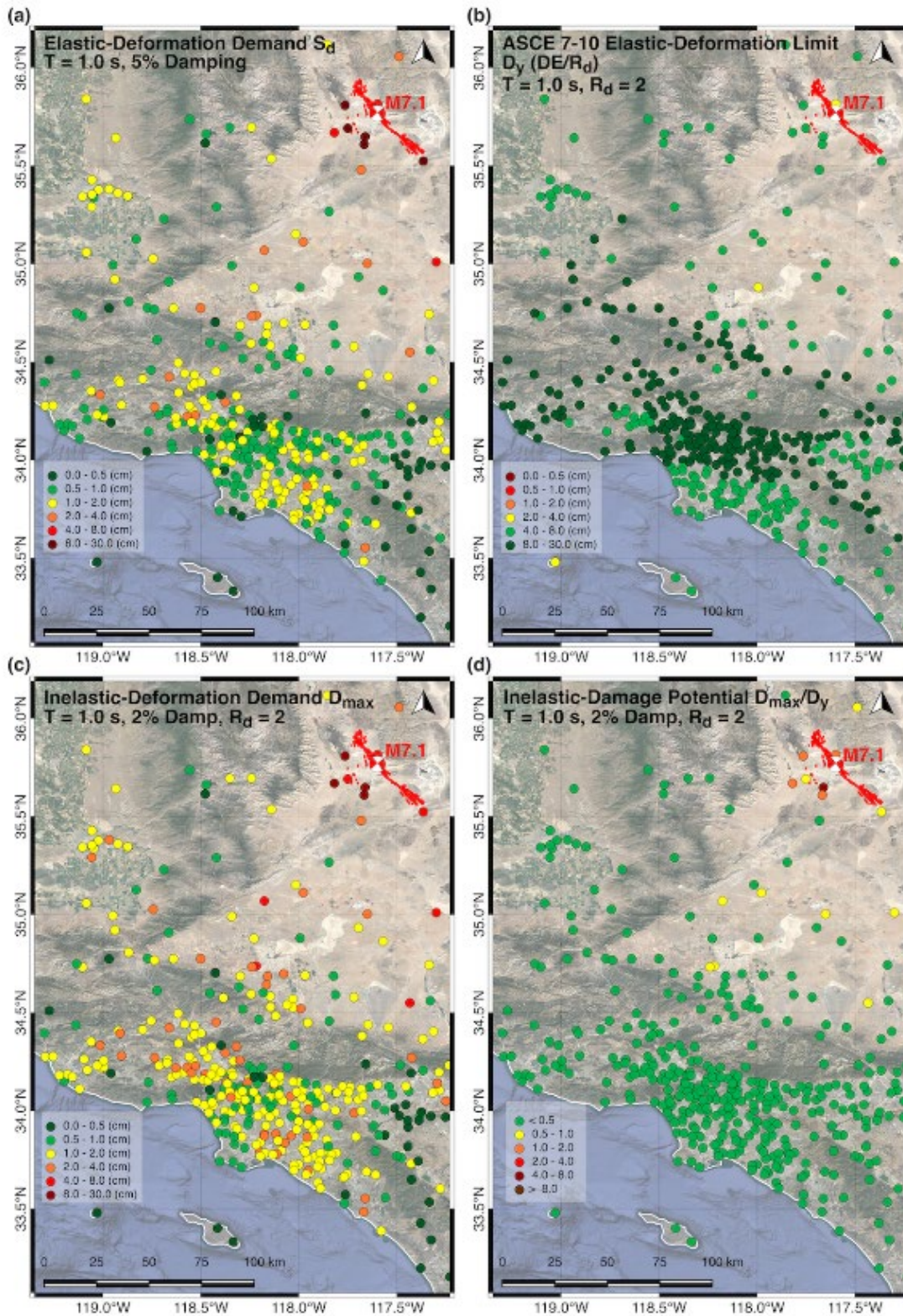
and far from faults).

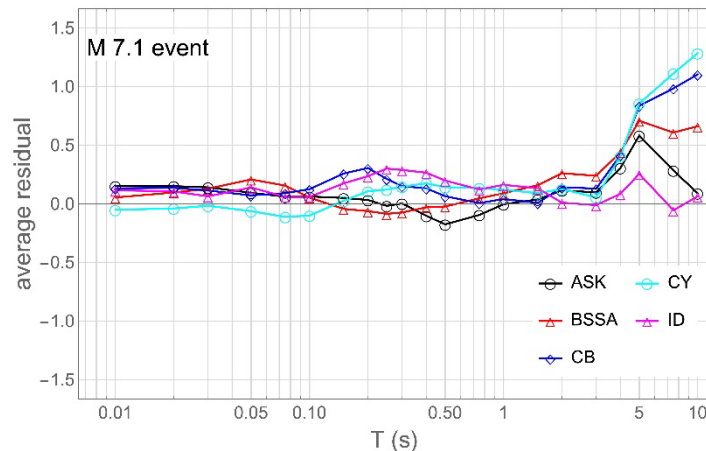**Figure 4**. Deformation response of elastic and inelastic models, $R_d = 2$ (Ahdi et al, 2020).

Figure 5. Event terms (average residuals) for the **M**7.1 main shock and the five NGA-West2 models vs. spectral period (Ahdi, et al., 2020).

Acknowledgements

References

Abrahamson, N. A., W.J. Silva, and R. Kamai (2014). Summary of the ASK14 ground motion relation for active crustal regions, *Earthq. Spectra*, **30**(3), 1025–1055.

Ahdi, S.K., S. Mazzoni, T. Kishida, P. Wang, C.C. Nweke, J.P. Stewart, and Y. Bozorgnia (2019). Processed ground motion recordings of the 2019 Ridgecrest Earthquake Sequence, *Report of the Natural Hazards Risk and Resiliency Research Center (NHR3), B. John Garrick Institute for the Risk Sciences, University of California, Los Angele*s. https://www.risksciences.ucla.edu/nhr3/gmdata/2019-ridgecrest-earthquake-sequence.

Ahdi, S.K., S. Mazzoni, T. Kishida, P. Wang, C.C. Nweke, N.M. Kuehn, V. Contreras, B. Rowshandel, J.P. Stewart, and Y. Bozorgnia (2020). Engineering Characteristics of Ground Motions Recorded in the 2019 Ridgecrest Earthquake Sequence, *Bull. Seismol. Soc. Am*, **110**(4), 1474-1494.

Ahdi, S.K., S. Sadiq, O. Ilhan, Y. Bozorgnia, Y.M.A. Hashash, D.Y. Kwak, D. Park, A. Yong, and J.P. Stewart (2018). Development of a United States Community Shear Wave Velocity Profile Database, *in 5th Conference on Geotechnical Earthquake Engineering and Soil Dynamics (GEESD-V)*, eds. S.J. Brandenberg and M.T. Manzari, Austin, TX, USA, 10–13 June 2018, 330–339.

ASCE (2010). Minimum Design Loads for Buildings and Other Structures, *American Society of Civil Engineers Standard ASCE/SEI 7-10*, Reston VA.

ASCE (2016). Minimum Design Loads and Associated Criteria for Buildings and Other Structures, *American Society of Civil Engineers Standard ASCE/SEI 7-16*, Reston, VA.

Boore, D.M. (2010). Orientation-independent, non-geometric-mean measures of seismic intensity from two horizontal components of motion, *Bull. Seism. Soc. Am.* **100**(4), 1830–1835.

Boore, D.M., Stewart, J.P., Seyhan, E., and Atkinson, G.M. (2014). NGA-West2 equations for predicting PGA, PGV, and 5% damped PSA for shallow crustal earthquakes, *Earthq. Spectra*, **30**(3), 1057–1085.

Campbell, K.W., and Y. Bozorgnia (2014). NGA-West2 ground motion model for the average horizontal components of PGA, PGV, and 5% damped linear acceleration response spectra, *Earthq. Spectra*, **30**(3), 1087–1115.

Chiou, B.S.-J., and R.R. Youngs (2014). Update of the Chiou and Youngs NGA model for the average horizontal component of peak ground motion and response spectra, *Earthq. Spectra*, **30**(3), 1117–1153.

DuRoss, C.B., R.D. Gold, Dawson, T.E., K.M. Scharer, K.J. Kendrick, S.O. Akciz, et al. (2020). Surface Displacement Distributions for the July 2019 Ridgecrest, California, Earthquake Ruptures; *Bull Seismol Soc Am.*, **110**(4), 1400–1418.

GEER (2019); Stewart, J.P. (ed.), S.J. Brandenberg, P. Wang, C.C. Nweke, K.S. Hudson, S. Mazzoni, Y. Bozorgnia, C.A. Goulet, K.W. Hudnut, C.A. Davis, S.K. Ahdi, F. Zareian, J. Fayaz, R.D. Koehler, C. Chupik, I. Pierce, A. Williams, S. Akciz, M.B. Hudson, T. Kishida, B. Brooks, R. Gold, D. Ponti, K. Scharer, D. McPhillips, C. DuRoss, T. Ericksen, J. Hernandez, J. Patton, B. Olson, T. Dawson, J. Treiman, K. Blake, J. Bachhuber, C. Madugo, J. Sun, A. Donnellan, G. Lyzenga, and E. Conway. *2019 Ridgecrest Earthquake Sequence. Geotechnical Extreme Event Reconnaissance (GEER) Association Report* GEER-064, https://doi.org/10.18118/G6H66K, 7/19/2019, Revised 8/1/2019.

Idriss, I.M. (2014). An NGA-West2 empirical model for estimating the horizontal spectral values generated by shallow crustal earthquakes, *Earthq. Spectra*, **30**(3), 1155–1177.

Iwahashi, J., and R.J. Pike (2007). Automated classifications of topography from DEMs by an unsupervised nested-means algorithm and a three-part geometric signature, *Geomorphology*, **86**, 409–440.

Louie, J.N. (2001). Faster, better: Shear-wave velocity to 100 meters depth from Refraction Microtremor Arrays, *Bull. Seismol. Soc. Am.*, **91**(2), 347–364.

McKenna, F., M.H. Scott, and G.L. Fenves (2010). "Nonlinear finite-element analysis software architecture using object composition." *J. Comput. Civ. Eng.*, **24**(1), 95–107.

Nweke, C.C., P. Wang, S.J. Brandenberg, and J.P. Stewart (2018). Reconsidering basin effects in

ergodic site response models, *Proceedings of the 2018 California Strong Motion Instrumentation Program (CSMIP) Seminar on Utilization of Strong-Motion Data*, Sacramento, CA, 25 October 2018.

Seyhan, E., J.P. Stewart, T.D. Ancheta, R.B. Darragh, R.W. and Graves (2014). NGA-West2 site database, *Earthq. Spectra*, **30**, 1007–1024.

Small, P., D. Gill, P.J. Maechling, R. Taborda, S. Callaghan, T.H. Jordan, G.P. Ely, K.B. Olsen, and C.A. Goulet (2017). The SCEC Unified Community Velocity Model Software Framework. *Seismol. Res. Lett.*, **88**(5), 1539–1552.

Thompson, E.M. (2018). An Updated Vs30 Map for California with Geologic and Topographic Constraints: U.S. Geological Survey data release, https://doi.org/10.5066/F7JQ108S.

Thompson, E.M., D.J. Wald, and C.B. Worden (2014). A V_{S30} map for California with geologic and topographic constraints, *Bull. Seismol. Soc. Am.,* **104**, 2313–2321.

Wald, D.J. and T.I. Allen (2007). Topographic slope as a proxy for seismic site conditions and amplification, *Bull. Seismol. Soc. Am.*, **97**, 1379–1395.

Wills, C.J., C.I. Gutierrez, F.G. Perez, and D.M. Branum (2015). A next generation VS30 map for California based on geology and topography, *Bull. Seismol. Soc. Am.*, **105**, 3083–3091.

Yong, A. (2016). Comparison of measured and proxy-based V_{S30} values in California, *Earthq. Spectra,* **32**,W 171–192.

Yong, A., E.M. Thompson, D.J. Wald, K.L. Knudsen, J.K. Odum, J.K., W.J. Stephenson, and S. Haefner (2016). Compilation of V_{S30} Data for the United States: U.S. Geological Survey Data Series 978, 8 p., http://dx.doi.org/10.3133/ds978.